Electrochimica Acta 133 (2014) 197–208

Contents lists available at ScienceDirect

Electrochimica Acta

journal homepage: www.elsevier.com/locate/electacta

Theoretical Analysis of Potential and Current Distributions in Planar Electrodes of Lithium-ion Batteries

Peyman Taheri[a,*], Abraham Mansouri[b], Maryam Yazdanpour[a], Majid Bahrami[a]

[a] Laboratory for Alternative Energy Conversion (LAEC), School of Mechatronic Systems Engineering, Simon Fraser University, Surrey, BC V3T 0A3, Canada
[b] Department of Mechanical Engineering, American University in Dubai, Dubai, 28282, UAE

ARTICLE INFO

Article history:
Received 5 April 2014
Accepted 7 April 2014
Available online 18 April 2014

Keywords:
Battery modelling
Lithium-ion battery
Battery ohmic loss
Electrode design
Polarization expression

ABSTRACT

An analytical model is proposed to describe the two-dimensional distribution of potential and current in planar electrodes of pouch-type lithium-ion batteries. A concentration-independent polarization expression, obtained experimentally, is used to mimic the electrochemical performance of the battery. By numerically solving the charge balance equation on each electrode in conjugation with the polarization expression, the battery behavior during constant-current discharge processes is simulated. Our numerical simulations show that reaction current between the electrodes remains approximately uniform during most of the discharge process, in particular, when depth-of-discharge varies from 5% to 85%. This observation suggests to simplify the electrochemical behavior of the battery such that the charge balance equation on each electrode can be solved analytically to obtain closed-form solutions for potential and current density distributions. The analytical model shows fair agreement with numerical data at modest computational cost. The model is applicable for both charge and discharge processes, and its application is demonstrated for a prismatic 20 Ah nickel-manganese-cobalt lithium-ion battery during discharge processes.

1. Introduction

There is a growing interest in development of practical models to describe chemical, electrical and thermal processes in Lithium-ion (Li-ion) batteries with thin-layer cell (electrode) assemblies. From the macroscopic point of view, the multi-physics processes in Li-ion cells can locally be divided into two distinct parts: *i*) the processes in the electrolyte (solution phase), and *ii*) the processes in the electrodes (solid phase). These processes are strongly coupled; the former involves the transport (migration, diffusion, and convection) of mass and charge between the electrodes through an electrolyte solution accompanied by interfacial reactions at the surface of electrodes, while the latter deals with transport (mostly via conduction) of charges within the solid phase of the electrode assembly, i.e., current collectors and active material particles. Both categories of processes involve thermal effects, which are not the focus of this work.

To describe the processes within the electrolyte solution an electrochemical model with kinetic boundary conditions is required [1]. The most well-known physics-based electrochemical model for Li-ion batteries is the porous-electrode model, proposed by Newman and co-workers [2–4], and its variations for different lithium-based chemistries and applications; for examples see Refs. [5–13]. Such detailed electrochemical models are quite useful for cell design and optimization, however, they are typically of very high-order and complexity and are not suitable for real-time applications, in particular for multi-dimensional calculations and/or for thermally coupled models [14]. Also, for the case of Li-ion cells, due to simple treatment of active material in the porous-electrode model, numerous transport properties are needed to fit experimental data [15]. More recently, reduced-order electrochemical models for Li-ion cells are introduced [14,16–19]. The order reduction decreases the computational time and allows the model implementation into a real-time on-board electronic control unit, which is of particular interest in vehicle applications to estimate lithium ion concentrations and associated state-of-charge values. Nonetheless, the simplified models neglect some dynamics so that they cannot accurately predict the current-voltage behavior across different operating conditions.

* Corresponding author. fax: +1 (778) 782 7514
E-mail addresses: ptaherib@sfu.ca (P. Taheri), mansouri@ualberta.net (A. Mansouri), myazdanp@sfu.ca (M. Yazdanpour), mbahrami@sfu.ca (M. Bahrami).

http://dx.doi.org/10.1016/j.electacta.2014.04.040
0013-4686/

Nomenclature

a	width of electrode (m)
b	width of electrode tab (m)
c	height of electrode (m)
$\mathcal{C}_l$	interpolation coefficients for Y_{ec}
$\mathcal{C}_T$	temperature coefficient for Y_{ec}
$\mathcal{D}_m$	interpolation coefficients for V_{oc}
$\mathcal{D}_T$	temperature coefficient for V_{oc}
e	distance of tab centre from y-axis (m)
i	in-plane current density ($A\,m^{-2}$)
I	applied current (A)
J	reaction current density ($A\,m^{-2}$)
$\mathbf{n}$	unit normal vector on elctrode
N	number of cells in battery core
Q	capacity (Ah)
R_{ec}	electrochemical resistance (Ωm^2)
t	time (s)
T	temperature (K)
V	potential (V)
V_{oc}	open-circuit potential (V)
x	horizontal position in Cartesian coordinate (m)
y	vertical position in Cartesian coordinate (m)
Y_{ec}	electrochemical conductance per unit area ($S\,m^{-2}$)

Greek

α_k	kth eigenvalue
δ	thickness (m)
ν	voltage transformation variable (V)
σ	electrical conductivity ($S\,m^{-1}$)

Subscript

am	related to active material
cc	related to current collector
elec	related to electrode
eff	effective value of a property
batt	related to battery
cell	related to cell (electrode pair)
n	related to the negative domain
p	related to the positive domain
ref	reference value
tab	related to electrode tab
x	related to x direction
y	related to y direction

Superscript

–	averaged value of a property
∼	shifted value of a property
max	maximum value of a property

When a battery exists and experimental data of the battery is available, empirical models which mimic the electrochemical performance of the battery can be generated. Empirical models are relatively fast and simple, thus are favored in control algorithms for battery management system [20]. Equivalent circuit models [21,22] and fitting function models [23,24] are common methodologies in this category.

In the present work, a simple concentration-independent polarization expression [23–25] is employed to describe the collective behavior of complex processes in the electrolyte solution between the electrodes. Standard constant-current discharge tests at a fixed environmental temperature are employed to determine the required coefficients in the polarization expression.

To model the overall battery performance, the processes in the electrolyte between the electrode must be linked to those which occur within the electrodes. For this, the governing equations, i.e., the charge balance equation coupled with the polarization expression, must be solved on each electrode. Based on this approach, several numerical analyses have been presented to describe the effects of electrode configuration on current and potential distributions inside the battery [26,27], and investigate the thermal effects in different operating conditions [28–32].

Similar to the above-mentioned studies, in the present work, the governing equations are solved numerically to obtain two-dimensional distributions of reaction current through the electrolyte, along with potential and current density distributions on the electrodes. However, the contribution of the authors to the subject is the development of a new "analytical" solution for this problem, which makes this work superior from the computational perspective. The key observation from our numerical simulations was that the processes in the electrolyte can be simplified such that the governing equations can be decoupled and an analytical solution for potential and current distribution on the electrodes can be derived. The proposed theoretical model and its implementation on an experimental pouch-type Li-ion battery are discussed in detail. The results are compared to numerical data with a fair agreement.

2. Formulation of the Problem

Figure 1a schematically shows the core of a pouch-type lithium-ion battery that is constructed of several cell assemblies, also known as electrode assemblies. In Fig. 1b, a single cell assembly is depicted. For better illustration, different layers in the cell assembly are shown separated. Each cell assembly includes a negative electrode, two separator sheets, and a positive electrode. The electrodes include active materials coated on both sides of current collector foils. Various active materials can be applied on electrodes depending on the chemistry of the Li-ion cell. In most Li-ion batteries, the current collector in positive and negative electrodes are foils of aluminum and copper, respectively. The separator sheet is an electrically inert membrane for transportation of cations (Li^+) between the electrodes. All layers, except current collectors, are porous and are soaked in a concentrated electrolyte liquid. The electrode tabs are the current collector foils extending outside the electrode plates for the purpose of electrical connection, and they are not covered by active materials.

Arrows in Fig. 1 present current streamlines during discharge processes. The through-plane straight arrows represent the transport of lithium ions (Li^+) between the electrodes, refereed to as "reaction current". The in-plane arrows in $x-y$ plane represent the transport of electric charges (e^-), i.e., the electrical current, on the electrode layers.

For convenience, the reaction current on both sides of each electrode in a single cell assembly can be considered to occur on one side of the electrode, as shown in Fig. 2. Consequently, the thicknesses of active material layers and the separator sheet in Fig. 2 are doubled.

A dimensional analysis can be performed to show that owing to the small thickness of layers in the cell assembly, compared to their dimensions in x and y directions, the distribution of potential in the electrodes is two-dimensional in $x-y$ plane [13]. Accordingly, the governing differential equation for the charge balance in each electrode reads

$$\sigma_{\mathrm{eff},j}\left(\frac{\partial^2 V_j}{\partial x^2}+\frac{\partial^2 V_j}{\partial y^2}\right)+\frac{\mathbf{J}\cdot\mathbf{n}_j}{\delta_{\mathrm{elec},j}}=0 \quad (j=p,n) \tag{1}$$

where x and y indicate the Cartesian coordinate system (m), and $V_j = V_j(x, y)$ is the two-dimensional potential distribution in the

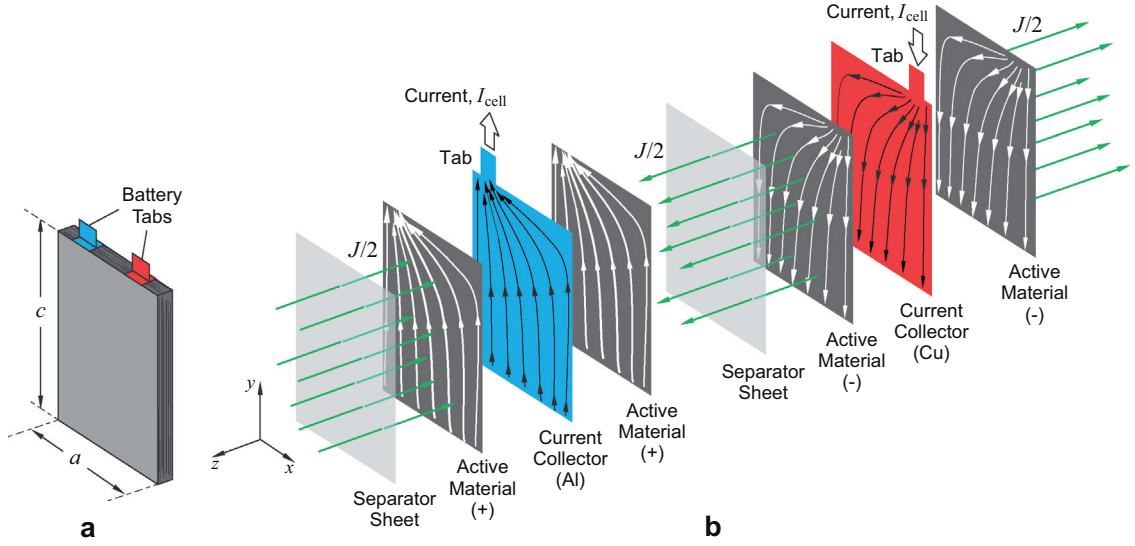

Fig. 1. a) Core (electrode-separator stack) of a prismatic lithium-ion battery with planar electrodes is shown. b) Schematic of a cell assembly in the battery is shown. The battery core is constructed of several cell assemblies. Different layers of the cell are separated for the sake of presentation. The arrows in z direction correspond to reaction current, the transport of Li^+ from the negative electrode to the positive electrode during a discharge process. The arrows in x-y plane are current streamlines on electrodes.

electrodes (V). The subscript j indicates the properties in negative ($j=n$) and positive ($j=p$) electrodes. Domains of the negative and positive electrodes are denoted by Ω_n and Ω_p, respectively. The reaction current density vector on the electrodes is $\mathbf{J}=\{J_x, J_y, J\}$ in ($A\,m^{-2}$), where J_x and J_y are side reactions and are considered to be negligible. The through-plane component of the reaction current J corresponds to the intercalation of lithium ions in the electrodes. The electrode thickness in z direction is $\delta_{elec,j}$ in (m), and $\mathbf{n}_j$ is the unit normal vector on each electrode surface pointing outward; $\mathbf{n}_p=\{0, 0, -1\}$ and $\mathbf{n}_n=\{0, 0, +1\}$.

The quantity $\sigma_{eff,j}$ is the effective electrical conductivity ($S\,m^{-1}$) of each electrode. The concept of *equivalent resistance network* is employed to define an effective electrical conductivity for each multilayered electrode [33,34]. Based on Fig. 1, there are parallel resistors in x and y directions, thus

$$\sigma_{eff,j}=\frac{1}{\delta_{elec,j}}\left(\delta_{cc,j}\,\sigma_{cc,j}+2\delta_{am,j}\,\sigma_{am,j}\right)\quad(j=p,n)$$

with

$$\delta_{elec,j}=\delta_{cc,j}+2\delta_{am,j}\quad(j=p,n)$$

where $\delta_{cc,j}$ and $\delta_{am,j}$ are thicknesses of the current collector sheet and the layer of active material, respectively. Electrical conductivity of the current collector and the active material are denoted by σ_{cc} and σ_{am}. Note that in the calculation of effective electrical conductivities, separator sheets are not considered since they are electrically inert.

As depicted in Fig. 3, each electrode can be considered as a rectangular domain in x-y plane of width a and height c. The through-plane current enters (or exits) the domain through its surface in x-y plane, whereas the in-plane current is allowed to enter (or exit) the domain through the tab constriction of width b on the boundary at $y=c$. The distance between the centre of the tab and y-axis is denoted by e_j.

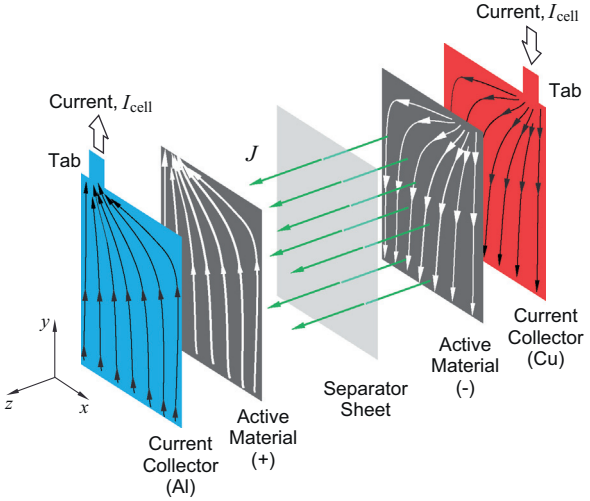

Fig. 2. Schematic of a the simplified cell assembly.

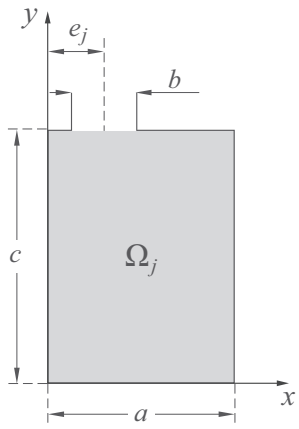

Fig. 3. Two-dimensional schematic of planar electrodes. Width and height of electrodes and width of the electrode tab are the same for both positive and negative electrodes. The distance of the tab centre from y axis, denoted by e_j, differs between the electrodes.

With reference to Figs. 2 and 3, the relevant boundary conditions for Eq. (1) at the positive electrode are

$$-\sigma_{\text{eff},p}\frac{\partial V_p}{\partial x}=0 \quad \text{at} \quad x=0 \tag{2a}$$

$$-\sigma_{\text{eff},p}\frac{\partial V_p}{\partial x}=0 \quad \text{at} \quad x=a \tag{2b}$$

$$-\sigma_{\text{eff},p}\frac{\partial V_p}{\partial y}=0 \quad \text{at} \quad y=0 \tag{2c}$$

$$-\sigma_{\text{eff},p}\frac{\partial V_p}{\partial y}=i_{\text{tab},p} \quad \text{at} \quad e_p-\frac{b}{2}<x<e_p+\frac{b}{2}, \quad y=c \tag{2d}$$

$$-\sigma_{\text{eff},p}\frac{\partial V_p}{\partial y}=0 \quad \text{at} \quad e_p+\frac{b}{2}<x<e_p-\frac{b}{2}, \quad y=c \tag{2e}$$

Similarly, for the negative electrode

$$-\sigma_{\text{eff},n}\frac{\partial V_n}{\partial x}=0 \quad \text{at} \quad x=0 \tag{3a}$$

$$-\sigma_{\text{eff},n}\frac{\partial V_n}{\partial x}=0 \quad \text{at} \quad x=a \tag{3b}$$

$$-\sigma_{\text{eff},n}\frac{\partial V_n}{\partial y}=0 \quad \text{at} \quad y=0 \tag{3c}$$

$$V_n=0 \quad \text{at} \quad e_n-\frac{b}{2}<x<e_n+\frac{b}{2}, \quad y=c \tag{3d}$$

$$-\sigma_{\text{eff},n}\frac{\partial V_n}{\partial y}=0 \quad \text{at} \quad e_n+\frac{b}{2}<x<e_n-\frac{b}{2}, \quad y=c \tag{3e}$$

The above boundary conditions imply that no current passes through boundaries of Ω_p and Ω_n except for the tab boundaries. In Eq. (2d), $i_{\text{tab},p}$ is the in-plane current density (A m^{-2}) at the tab of positive electrode

$$i_{\text{tab},p}=\frac{I_{\text{cell}}}{b\,\delta_{\text{elec},p}} \tag{4}$$

where I_{cell} is the applied current (A) of the cell (electrode) assembly, and $b\,\delta_{\text{elec},p}$ is the cross-sectional area of the positive tab. In Eq. (3d), potential at the tab boundary of the negative electrode is set to zero in order to provide a reference for potential distribution [25,26].

Once the boundary-value problem, i.e., Eqs. (1)–(2), is solved, Ohm's law can be used to find the in-plane current density vector, $\mathbf{i}_j=\{i_x, i_y, 0\}_j$, on each electrode where

$$i_{x,j}=-\sigma_{\text{eff},j}\frac{\partial V_j}{\partial x} \quad \text{and} \quad i_{y,j}=-\sigma_{\text{eff},j}\frac{\partial V_j}{\partial y} \quad (j=p,n) \tag{5}$$

3. Experimental Battery

For experimentation, we use a 20 Ah pouch-type Li-ion battery (EiG Battery, South Korea). An image from the layered structure of the battery core, i.e., electrode-separator stack, is depicted in Fig. 4a. Lithiated nickel-manganese-cobalt oxides and lithiated graphite are used as active materials at positive and negative electrodes, respectively. In Fig. 4b, laminated structure of a negative electrode is shown; a layer of active material coated on both sides of a copper foil (one side is shown), compare with Fig. 1.

The experimental battery includes 18 cell assemblies connected in parallel, with a z-fold design for the separator sheet. For parallel connection of the cells, electrode tabs of the same type are welded together to form the battery terminals. The electrode-separator stack is soaked in an aqueous electrolyte and packed in a pouch case with terminals extending outside the pouch, see Fig. 4c. A mixture of ethylene carbonate (EC) and diethyl carbonate (DEC) are the solvents and $LiPF_6$ is the solute for the electrolyte.

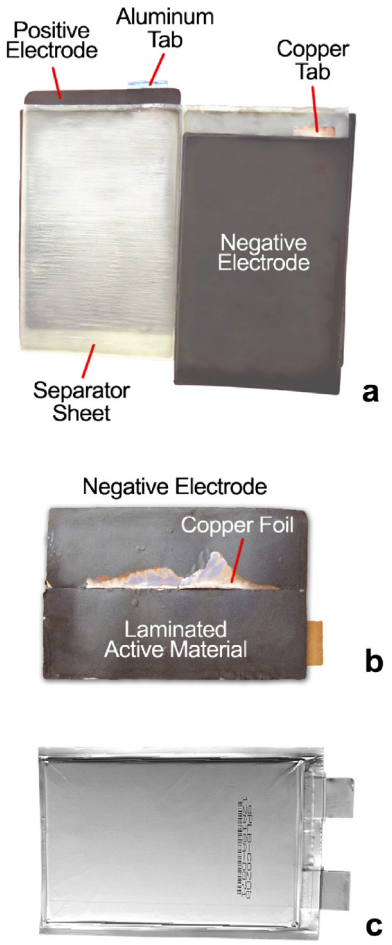

Fig. 4. a) Electrode-separator stack of the experimental battery. b) Layered structure of the negative electrode. c) The actual experimental battery with the pouch case.

With reference to Fig. 3, dimensions of the battery layers are given in Table 1. The thickness and electrical conductivity of battery components at the presence of electrolyte (wet) are listed in Table 2; compare with Fig. 1.

Voltage response of the experimental battery during discharge processes at various C-rates (0.3C, 0.5C, 1C, 2C, 3C, 4C, 5C and 6C) and at the temperature of 25 °C is shown in Fig. 5. The capacity at 1C-rate discharge is around 20 A h, which is used as the nominal capacity. The cutoff voltage of 3 V is set for discharge data, which is the typical voltage limit for Li-ion cells.

4. Polarization Expression

Distribution of the reaction current density J, is dictated by the local rate of electrochemical reactions in electrodes. For an accurate description of J a distributed electrochemical model must be employed [12,13]. In this study, instead of an electrochemical model, a mathematical model [23,24] is adapted to predict the time dependent distribution of the reaction current during constant-current discharge processes in the experimental Li-ion battery. The model uses experimentally determined polarization expressions to describe the overpotential between positive and negative electrodes.

Confirmed by experimental observations [24] and electrochemical simulations [11], at a fixed depth-of-discharge (DOD), the discharge voltage exhibits an approximately linear dependency on

Table 1
Dimensions of electrode domains Ω_p and Ω_n in x-y plane, corresponding to Fig. 3.

Electrode	a (m)	b (m)	c (m)	e (m)
Positive	125×10^{-3}	30×10^{-3}	195×10^{-3}	27.5×10^{-3}
Negative	125×10^{-3}	30×10^{-3}	195×10^{-3}	97.5×10^{-3}

Table 2
Thickness and electrical conductivity of components in the battery core.

Material/Layer	Thickness, δ (m)	Electrical conductivity, σ (S m^{-1})
Aluminum current collector	21×10^{-6}	37.8×10^{6}
Copper current collector	12×10^{-6}	59.6×10^{6}
Separator sheet	25×10^{-6}	-
Positive active material	70×10^{-6}	13.9 (wet)
Negative active material	79×10^{-6}	100 (wet)

current density. Accordingly, a linear polarization expression can be assumed as [23–25]

$$J(x,y) = Y_{ec}\left[V_p(x,y) - V_n(x,y) - V_{oc}\right] \tag{6}$$

Here, Y_{ec} is the electrochemical conductance, i.e., the conductance of separator and electrolyte per unit area (S m^{-2}), V_{oc} is the open-circuit (equilibrium) potential of the cell, and $V_p - V_n$ corresponds to the potential difference between two points on the positive and negative electrodes with the same coordinates in x-y plane. By convention, J assumes positive and negative values for charge and discharge processes, respectively. It needs to be emphasized that for charging, experimental data on charging processes are required, but the procedure explained below is still applicable [35].

The current of cell assembly I_{cell} and the current of battery I_{batt} are related to J via

$$I_{cell} = \int_0^a \int_0^c J(x,y)\, dy\, dx \quad \text{and} \quad I_{batt} = I_{cell}\, N \tag{7}$$

The number of cell assemblies inside the battery core [cf. Fig. 1a] is denoted by N. For the considered battery $N = 18$.

In the mathematical model, both Y_{ec} and V_{oc} are considered to solely depend on DOD, and their dependency is expressed in a polynomial form

$$Y_{ec} = \sum_{l=0}^{L} \mathcal{C}_l (\mathrm{DOD})^l \tag{8}$$

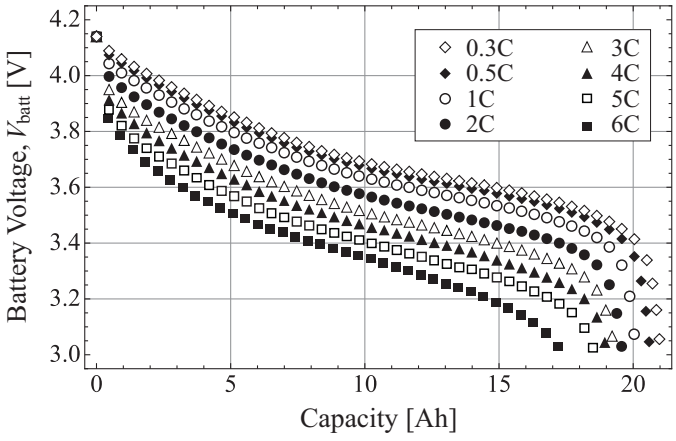

Fig. 5. Measured voltage response of the battery during constant-current discharge processes at different discharge rates at an environmental temperature of 25 °C.

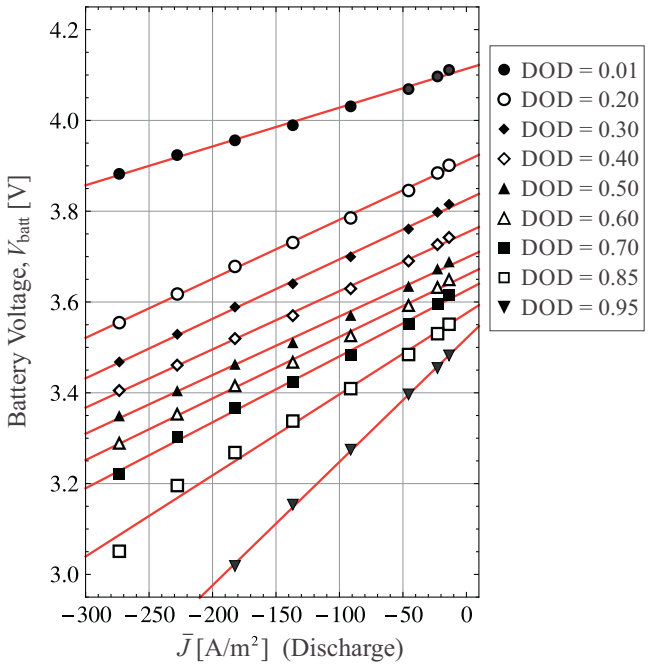

Fig. 6. The linear dependency of voltage and current at constant values of DOD.

$$V_{oc} = \sum_{m=0}^{M} \mathcal{D}_m (\mathrm{DOD})^m \tag{9}$$

where $\mathcal{C}_l$ and $\mathcal{D}_m$ are the constants to be determined from experimental voltage data during constant-current discharge processes.

DOD is defined as the fraction of cell capacity Q_{cell} (Ah), released during a discharge process. Given an initial DOD at $t = 0$ and assuming 100% coulombic efficiency, DOD (in %) can be calculated in time t (s) as

$$\mathrm{DOD}(t) = \mathrm{DOD}(0) + \frac{1}{3600\, Q_{cell}} \int_0^t \left| I_{cell}(t) \right| dt \tag{10}$$

where $Q_{cell} = Q_{batt}/N$ and the constant 3600 has the unit of second/hour.

To find coefficients $\mathcal{C}_l$ and $\mathcal{D}_m$, experimental data must be used to find the voltage values, V_{batt}, at different DOD stages during discharge processes at different currents. In Fig. 6, battery voltage variations are plotted against $\bar{J} = I_{cell}/(ac)$, which is the averaged value for J. As shown in the figure, at a constant DOD, variations of the battery voltage versus reaction current density, shown by symbols, can be approximated by a linear function (lines). In account for Eq. (6), Y_{ec} is the inverse of the line slope and V_{oc} is the intercept [24].

Plots in Fig. 7 depict the dependency of V_{oc}, Y_{ec}, and electrochemical resistance ($R_{ec} = Y_{ec}^{-1}$) on DOD, obtained from voltage measurements [cf. Fig. 5] and the above-mentioned procedure. Solid lines present fifth-order polynomial fits to the calculated values (symbols). The coefficients $\mathcal{C}_l$ and $\mathcal{D}_m$ for these polynomials are listed in Table 3. To show the accuracy of our calculations, predictions for V_{oc} are compared to voltage response of the battery during a 0.3C-rate (6 A) discharge; as shown, marginal deviations is expected due to the small applied current and the corresponding polarization loss.

4.1. Remarks on the Polarization Expression

One may argue that an inconsistency exists when V_{oc} and Y_{ec} are calculated from linear fittings to the experimental data using

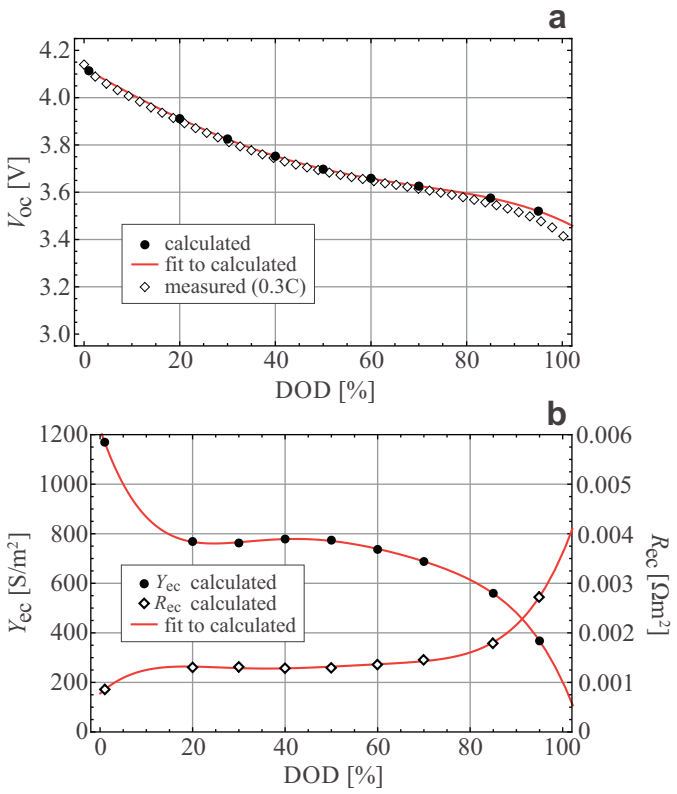

Fig. 7. a) The dependency of open-circuit potential V_{oc} on DOD. b) The dependency of electrochemical conductance Y_{ec} and electrochemical resistance R_{ec} on DOD.

Eq. (6), because an averaged reaction current density, $\bar{J}$, is used to interpret the experimental data (see Fig. 6) while in Eq. (6), J is not averaged.

We shall emphasize that the polarization expression proposed by Gu [cf. Eq. (6)], is ideal for small electrodes with wide tabs. In his experiments [24], Gu used 2.54 × 2.85 cm electrodes with full-length tabs, i.e., $b = a$ and $e_j = a/2$. Indeed, as the size of electrodes increases and size of the tabs decreases, the distribution of J deviates from a uniform distribution, however, as shown in the proceeding section, the polarization expression still can be used to approximate the current density distribution within the battery with a good accuracy.

To account for temperature effects in the polarization expression, dependency of the electrochemical conductance and open-circuit potential on temperature must be considered. According to Arrhenius equation which gives the relationship between the electrochemical reaction rate constant and the temperature, a temperature dependent Y_{ec} can be defined [32,36]

$$Y_{ec} = Y_{ec,\,ref}\,\mathrm{Exp}\left[\mathcal{C}_T\left(\frac{1}{T}-\frac{1}{T_{ref}}\right)\right] \tag{11}$$

Table 3
Coefficients for Y_{ec} and V_{oc} polynomials in Eqs. (8) and (9).

$\mathcal{C}_l$	Value (S m^{-2})	$\mathcal{D}_m$	Value (V)
$\mathcal{C}_0$	1222.7182993203342	$\mathcal{D}_0$	4.125111038010919
$\mathcal{C}_1$	-5561.683264570421	$\mathcal{D}_1$	-1.149003551480252
$\mathcal{C}_2$	24608.29562897738	$\mathcal{D}_2$	0.22963961100129981
$\mathcal{C}_3$	-49560.06383877925	$\mathcal{D}_3$	1.009817462684071
$\mathcal{C}_4$	46409.897374573746	$\mathcal{D}_4$	-0.41256347497735385
$\mathcal{C}_5$	-16916.711919087687	$\mathcal{D}_5$	-0.3239783290867153

Furthermore, Nernst equation which gives the relationship between the equilibrium potential and the temperature can be used to describe the Seebeck effect on V_{oc} [32,36]

$$V_{oc} = V_{oc,\,ref} + \mathcal{D}_T\,(T - T_{ref}) \tag{12}$$

where T is the battery temperature (K). The coefficients $\mathcal{C}_T$ and $\mathcal{D}_T$ are constants that must be determined from experiment [32,36] to fit the temperature dependence of Y_{ec} and V_{oc}. The subscript 'ref' denotes values at a reference temperature T_{ref}.

5. Numerical Analysis

A numerical analysis must be employed to solve Eq. (1) along with boundary conditions (2) and (3), because the governing Poisson equations [cf. Eq. (1)] for positive and negative domains are non-homogeneous and strongly coupled via their source terms.

In the present work, MUMPS (MUltifrontal Massively Parallel sparse direct Solver), integrated in COMSOL MULTIPHYSICS finite element PDE solver (Version 4.3b), is used to simultaneously solve Eqs. (1)–(3) and (6) over two separated domains, Ω_p and Ω_n, to evaluate $V_p(x, y)$, $V_n(x, y)$, and $J(x, y)$ at different DOD values.

5.1. Numerical Results

Once the potential distribution on positive and negative electrodes is obtained, the battery voltage V_{batt}, can be calculated as

$$V_{batt} = V_{tab,p} - V_{tab,n} = \frac{1}{b}\int_{e_p-\frac{b}{2}}^{e_p+\frac{b}{2}} V_p\,(x, c)\,dx \tag{13}$$

In Fig. 8, voltage response of the battery at different discharge rates, calculated numerically, is compared to experimental voltage values, i.e., data in Fig. 5. The comparison shows an excellent agreement between modelling results and measured values. However, when extreme discharge currents (>10C-rate) are involved, some issues may arise in evaluation of the polarization coefficients ($\mathcal{C}$ and $\mathcal{D}$). At higher discharge rates, the battery voltages V_{batt} reaches the cutoff voltage at lower values of DOD, thus voltage data at high DOD values are not available for the purpose of data fitting. This shortcoming is apparent in Fig. 6; voltage values for 5C-rate and 6C-rate are not available at DOD=95%.

Note that since electrodes inside the battery are connected in parallel, $V_{batt} = V_{cell}$.

In Fig. 9, plots (a) and (b) respectively correspond to potential distribution and current streamlines on the negative and positive electrodes at $t = 60$s (DOD = 5%) during a 3C-rate discharge process. Variation of potential on the surface of electrodes, which are at the order of millivolt, correspond to materials ohmic resistivity. The position of tabs on each electrode is indicated by the gray rectangle on the top edge of the domain. The magnitude of potential is shown with colours, black lines are equipotential lines, and white lines are current streamlines. Postulated by Eq. (5), equipotential lines and streamlines are perpendicular all over the domain.

During a constant-current discharge, no significant change in the pattern of potential and current distribution was observed in our numerical simulations. The local magnitude of the potential remains almost constant in the negative electrode for all DOD values. However, variation of local potential on the positive electrode is in the order of the battery voltage drop. This is because a significant portion of the total potential drop is associated with electrochemical resistance R_{ec}, but not the ohmic resistance in the electrodes.

In Fig. 10, the magnitude of in-plane current density distribution on negative and positive electrodes is shown, calculated from

$$\left|i\right|_j = \sqrt{i_{x,j}^2 + i_{y,j}^2} \quad (j = p, n) \tag{14}$$

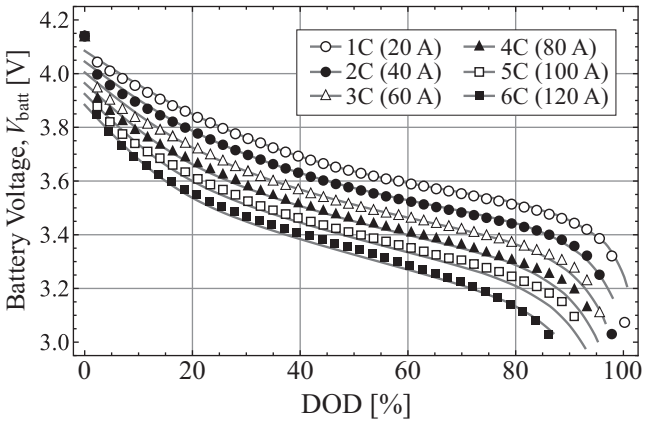

Fig. 8. Variation of battery voltage versus depth-of-discharge (DOD) for different discharge currents are shown. Symbols correspond to measured values and lines represent numerically calculated values.

The large magnitude of the in-plane current density corresponds to the small thickness of electrodes. Sudden increase of current density occurs near the tab due to constriction of the current flow at the tabs. At high discharge rates, this phenomena leads to high Joule heating and temperature rise near the tabs [28], which in turn increases the rate of electrochemical reactions and the risk of thermal runaway [37]. Note that since boundary conditions at the positive and negative tabs are different, current densities at the tabs exhibit some dissimilarities in the pattern.

Plots (a) to (c) in Fig. 11 show distributions of the normalized reaction current density, $J/\bar{J}$, between the electrodes at different DOD values during a 3C-rate discharge process. When $J/\bar{J} \to 1$ the distribution of reaction current tends to be uniform, whereas its deviation from unity means it is unevenly distributed. As depicted, the distribution pattern for reaction current changes drastically. Our simulations confirm that for DOD$\lessapprox$5 % the reaction current density is considerably higher at the vicinity of tabs, see Fig. 11a. At 5 %$\lessapprox$DOD$\lessapprox$85 % the distribution of reaction current becomes more uniform but still remains slightly higher near the tabs [cf. Fig. 11b]. However, near the end of discharge process, i.e., for DOD$\gtrapprox$85 %, when active materials are depleted at the top side of the electrodes near the tabs, the reaction current is forced away from the tabs towards the bottom of current collectors where active materials are less utilized; see Fig. 11c. We observed the same behaviour at all discharge currents (not shown here), nonetheless, such non-uniformities in reaction current become stronger at higher discharge rates.

To examine the uniformity of reaction current at different discharge rates, minimum and maximum values of $|J|$ with respect to DOD are obtained numerically and plotted in Fig. 12; solid lines represent the maximum values, long-dashed lines denote minimum values, and the averaged value, $|\bar{J}|$, is depicted by short-dashed lines. The plots reveal that within a large range of DOD, the reaction current varies slightly around its averaged value.

6. Theoretical Analysis

Results from the numerical analysis confirm that the reaction current is not uniformly distributed over the electrodes; however, its local variations are not drastic during most of the discharge process. Accordingly, a uniform reaction current density, $\bar{J}$, is superimposed in our analysis which allows to develop a theoretical model and describe the potential and current distributions on the electrodes with a closed-form expression. A similar assumption is proposed by Doyle and Newman [38] for development of an

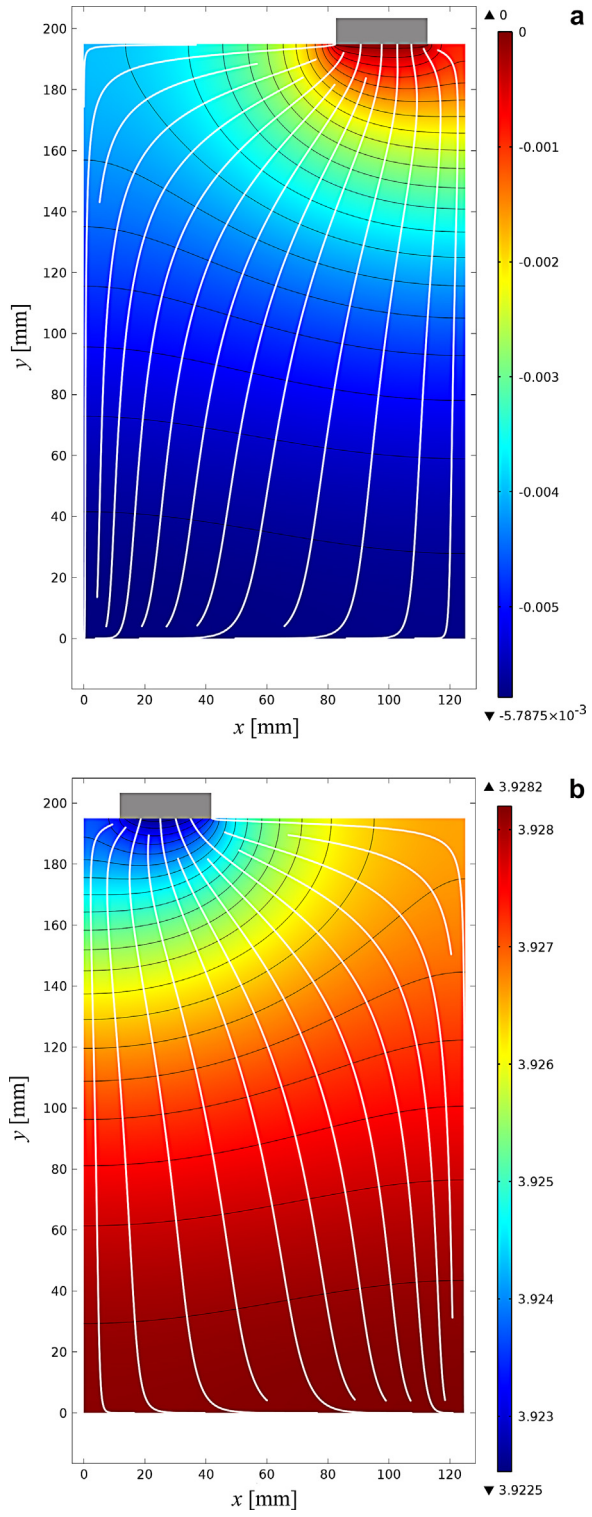

Fig. 9. The potential distribution and current streamlines on electrodes is shown during a 3C-rate discharge process at DOD = 5%. Plots (a) and (b) respectively correspond to potential distribution on the negative electrode V_n and potential distribution on the positive electrode V_p. Potential magnitude is shown with contours (colour maps with equipotential black lines) and current streamlines are depicted with white lines. Electrode tabs are indicated by gray rectangles on the top edge of the domain.

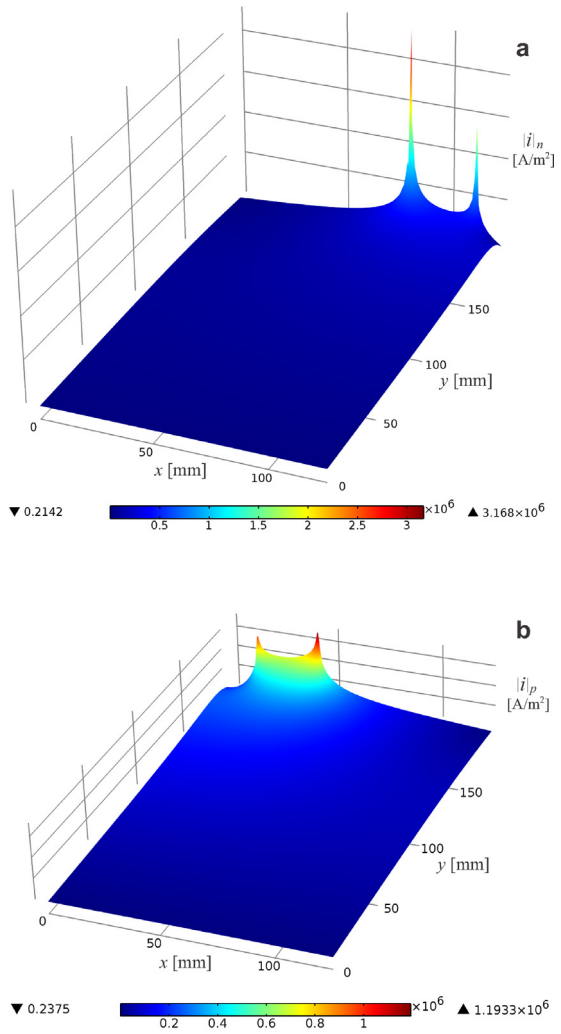

Fig. 10. The magnitude of in-plane current density distribution on negative electrode (Plot a) and positive electrode (Plot b) is shown during a 3C-rate discharge process at DOD = 5%. Sharp increase of current density occurs at the vicinity of electrode tabs due to constriction resistance.

analytical electrochemical model. Note that uniformity of reaction current density is a desired feature for Li-ion batteries, as it means that active material are evenly utilized, thus the battery degradation rate is minimized.

We define a new variable to transform the governing Poisson equation, Eq. (1), and the corresponding boundary conditions, Eqs. (2) and (3), into a Laplace equation, for which an analytical solution is accessible with the method of separation of variables. Let us introduce v, that relates V to $\bar{\mathbf{j}} \cdot \mathbf{n}$ via

$$V_j(x,y) = v_j(x,y) - \frac{1}{2}\frac{\bar{\mathbf{j}} \cdot \mathbf{n}_j}{\delta_{\text{elec},j}\,\sigma_{\text{eff},j}}\,y^2 \quad (j = p, n) \tag{15}$$

Substituting $V_j(x,y)$ from Eq. (15) into Eq. (1) and boundary conditions (2) and (3) yields the following homogeneous equation

$$\frac{\partial^2 v_j}{\partial x^2} + \frac{\partial^2 v_j}{\partial y^2} = 0 \quad (j = p, n) \tag{16}$$

with transformed boundary conditions for both electrodes ($j = p, n$)

$$\frac{\partial v_j}{\partial x} = 0 \quad \text{at} \quad x = 0 \tag{17a}$$

$$\frac{\partial v_j}{\partial x} = 0 \quad \text{at} \quad x = a \tag{17b}$$

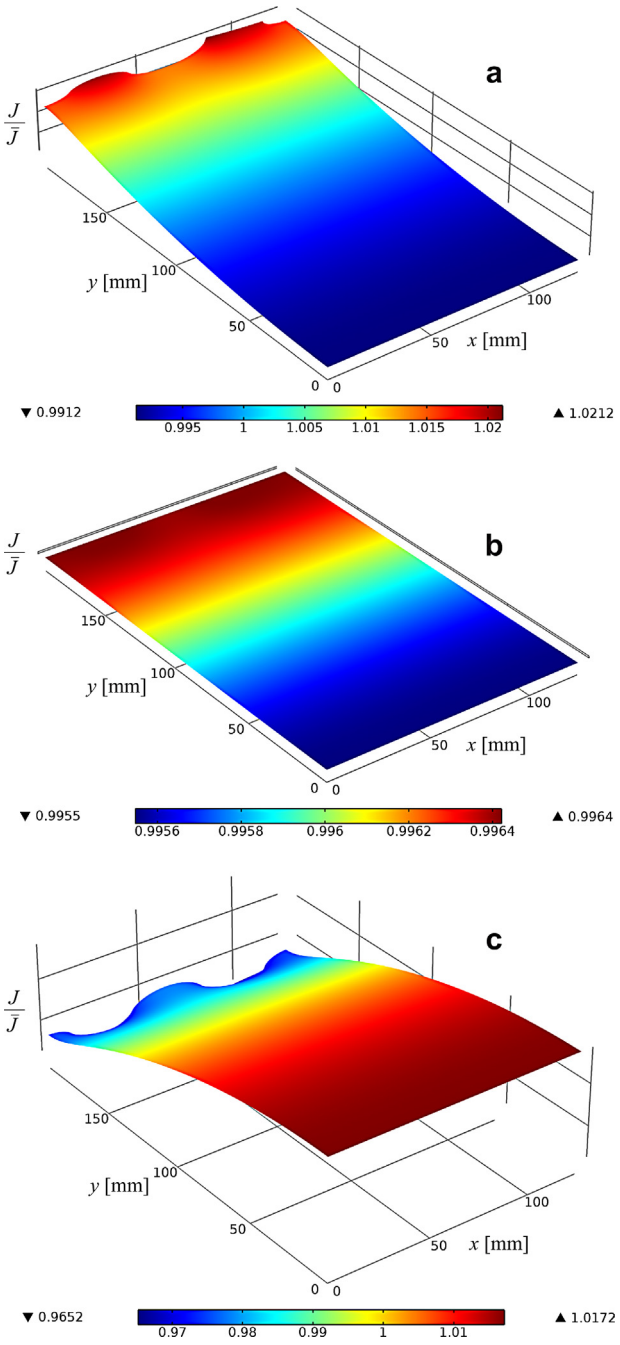

Fig. 11. Distribution of the normalized reaction current density between the electrodes is shown for a 3C-rate discharge at: a) DOD = 5%, and b) DOD = 77%, and c) DOD = 93%.

$$\frac{\partial v_j}{\partial y} = 0 \quad \text{at} \quad y = 0 \tag{17c}$$

$$\frac{\partial v_j}{\partial y} = \frac{\left(\bar{\mathbf{j}} \cdot \mathbf{n}_j\right) c}{\delta_{\text{elec},j}\,\sigma_{\text{eff},j}}\left(1 - \frac{a}{b}\right) \quad \text{at} \quad e_j - \frac{b}{2} < x < e_j + \frac{b}{2}, \quad y = c \tag{17d}$$

$$\frac{\partial v_j}{\partial y} = \frac{\left(\bar{\mathbf{j}} \cdot \mathbf{n}_j\right) c}{\delta_{\text{elec},j}\,\sigma_{\text{eff},j}} \quad \text{at} \quad e_j + \frac{b}{2} < x < e_j - \frac{b}{2}, \quad y = c \tag{17e}$$

Note that in derivation of Eq. (17d) for the positive electrode, the cell discharge current I_{cell} is replaced with $\left(\bar{\mathbf{j}} \cdot \mathbf{n}_p\right) a\, c$, with

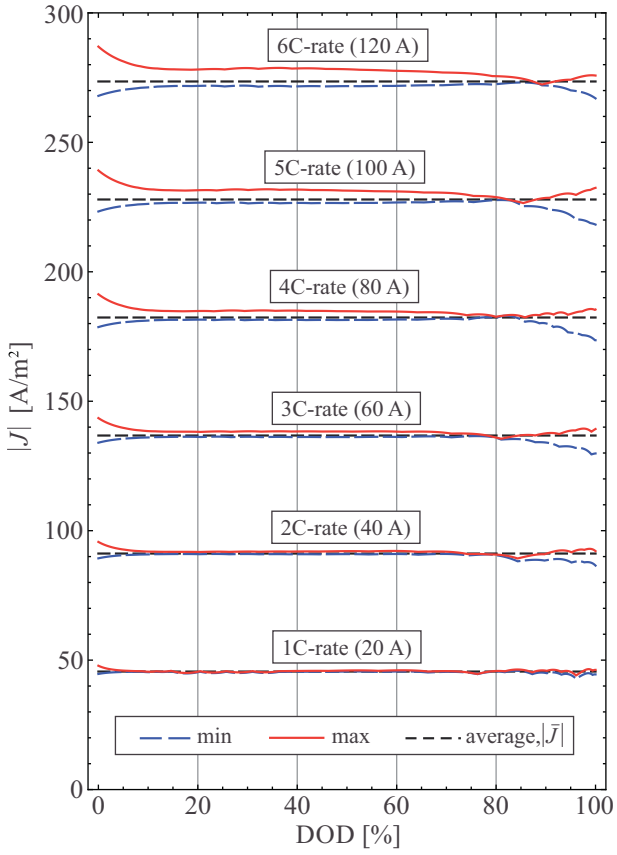

Fig. 12. Minimum, maximum, and averaged values of reaction current with respect to DOD are shown for different discharge rates.

reference to Eq. (7). Also, for the negative electrode an equivalent second-type (Neumann) boundary condition is introduced instead of the original first-type (Dirichlet) boundary condition, because the method of separation of variables with mixed boundary conditions cannot be applied on a Laplace equation [39]. For this reason a reference potential of zero cannot be prescribed in the analytical approach. Indeed, in the transformed system, the through-plane current density is eliminated from the source term of the original Poisson equation and its effects are reflected on the transformed boundary conditions.

Using the method of separation of variables, the general solution for Eq. (16) can be obtained as

$$v_j(x,y) = \sum_{k=1}^{\infty} A_{k,j} \cos(\alpha_k x) \cosh(\alpha_k y) \quad (j = p, n) \tag{18}$$

in which the summation is taken over all discrete spectrum of eigenvalues $\alpha_k = k\pi/a$. The terms $\cos(\alpha_k x)$ and $\cosh(\alpha_k y)$ are the eigenfunctions, and $A_{k,j}$ is the coefficient to be determined for each domain ($j = p, n$) from boundary conditions at $y = c$, i.e.

$$\sum_{k=1}^{\infty} A_{k,j}\alpha_k \cos(\alpha_k x) \sinh(\alpha_k c) = \begin{cases} \dfrac{(\bar{\mathbf{J}}\cdot\mathbf{n}_j)\,c}{\delta_{\text{elec},j}\,\sigma_{\text{eff},j}}\left(1-\dfrac{a}{b}\right) & \text{at} \quad e_j - \dfrac{b}{2} < x < e_j + \dfrac{b}{2} \\ \dfrac{(\bar{\mathbf{J}}\cdot\mathbf{n}_j)\,c}{\delta_{\text{elec},j}\,\sigma_{\text{eff},j}} & \text{at} \quad e_j + \dfrac{b}{2} < x < e_j - \dfrac{b}{2} \end{cases} \tag{19}$$

The unknown coefficient $A_{k,j}$ must be obtained from the orthogonality condition for eigenfunctions [39,40]

$$\int A_{k,j}\,\alpha_k \cos(\alpha_k x) \cos(\alpha_l x) \sinh(\alpha_k c)\,dx = 0 \quad \text{for} \quad k \neq l \tag{20}$$

Thus, multiplying both sides of Eq. (19) with $\cos(\alpha_l x)$ and subsequent integrating yields the following relation for $l = k$

$$\begin{aligned} &\int_0^a A_{k,j}\,\alpha_k \cos^2(\alpha_k x) \sinh(\alpha_k c)\,dx \\ &= \frac{(\bar{\mathbf{J}}\cdot\mathbf{n}_j)\,c}{\delta_{\text{elec},j}\,\sigma_{\text{eff},j}} \left[\int_0^{e_j - \frac{b}{2}} \cos(\alpha_k x)\,dx \right. \\ &\left. + \left(1-\frac{a}{b}\right) \int_{e_j-\frac{b}{2}}^{e_j+\frac{b}{2}} \cos(\alpha_k x)\,dx + \int_{e_j+\frac{b}{2}}^{a} \cos(\alpha_k x)\,dx \right] \end{aligned} \tag{21}$$

from which $A_{k,j}$ is evaluated as

$$A_{k,j} = \frac{4(\bar{\mathbf{J}}\cdot\mathbf{n}_j)\,c\left[b\sin(\alpha_k a) - 2a\cos\left(\alpha_k e_j\right)\sin\left(\alpha_k b/2\right)\right]}{\delta_{\text{elec},j}\,\sigma_{\text{eff},j}\,b\,\alpha_k \sinh(\alpha_k c)\left[2\alpha_k a + \sin(2\alpha_k a)\right]} \tag{22}$$

Finally, the solution for potential follows from Eq. (15)

$$V_j(x,y) = \sum_{k=1}^{\infty} A_{k,j} \cos(\alpha_k x) \cosh(\alpha_k y) - \frac{1}{2}\frac{\bar{\mathbf{J}}\cdot\mathbf{n}_j}{\delta_{\text{elec},j}\,\sigma_{\text{eff},j}}\,y^2 \tag{23}$$

Once the potential distribution is known, the in-plane current distribution can be obtained from Eq. (5).

The solution for potential distribution in Eq. (23) is the superposition of a one-dimensional potential distribution, $-\left(\bar{\mathbf{J}}\cdot\mathbf{n}_j\right)y^2/\left(2\delta_{\text{elec},j}\,\sigma_{\text{eff},j}\right)$, and a two-dimensional potential distribution, $\sum A_{k,j}\cos(\alpha_k x)\cosh(\alpha_k y)$. It is apparent that for $b = a$ and $e_j = a/2$, i.e., when a full length tab is used for the electrodes, the two-dimensional part of the solution vanishes, since $A_{k,j} = 0$.

6.1. Analytical Results

The analytical model was coded symbolically in MATHEMATICA (Wolfram Research, Version 8), which was also used to generate the plots.

As mentioned above, the analytical model does not allow a zero reference potential to be applied on the electrode boundary at the tabs. The absence of a reference potential in the analytical solution yields a positive potential on the negative electrode (with maximum at the tab) and a negative potential on the positive electrode (with minimum at the tab). However, the analytic solution allows one to easily find the maximum potential on the negative electrode, $V_n^{\max}$, and shift the potential distribution on both electrodes such that a reference potential of zero is set at the tab of negative electrode. The shifted potential distributions read

$$\tilde{V}_n(x,y) = V_n(x,y) - V_n^{\max} \tag{24}$$

and

$$\tilde{V}_p(x,y) = V_p(x,y) - V_n^{\max} + V_{\text{oc}} - \left(\bar{\mathbf{J}}\cdot\mathbf{n}_p\right)R_{\text{ec}} \tag{25}$$

where R_{ec} and V_{oc} are function of DOD; see Eqs. (8) and (9).

Note that the solution in Eq. (24) only accounts for the potential variation on the negative electrodes due to in-plane electrical resistivity, but the potential solution in Eq. (25) takes account for both in-plane electrical resistivity and the through-plane electrochemical resistivity.

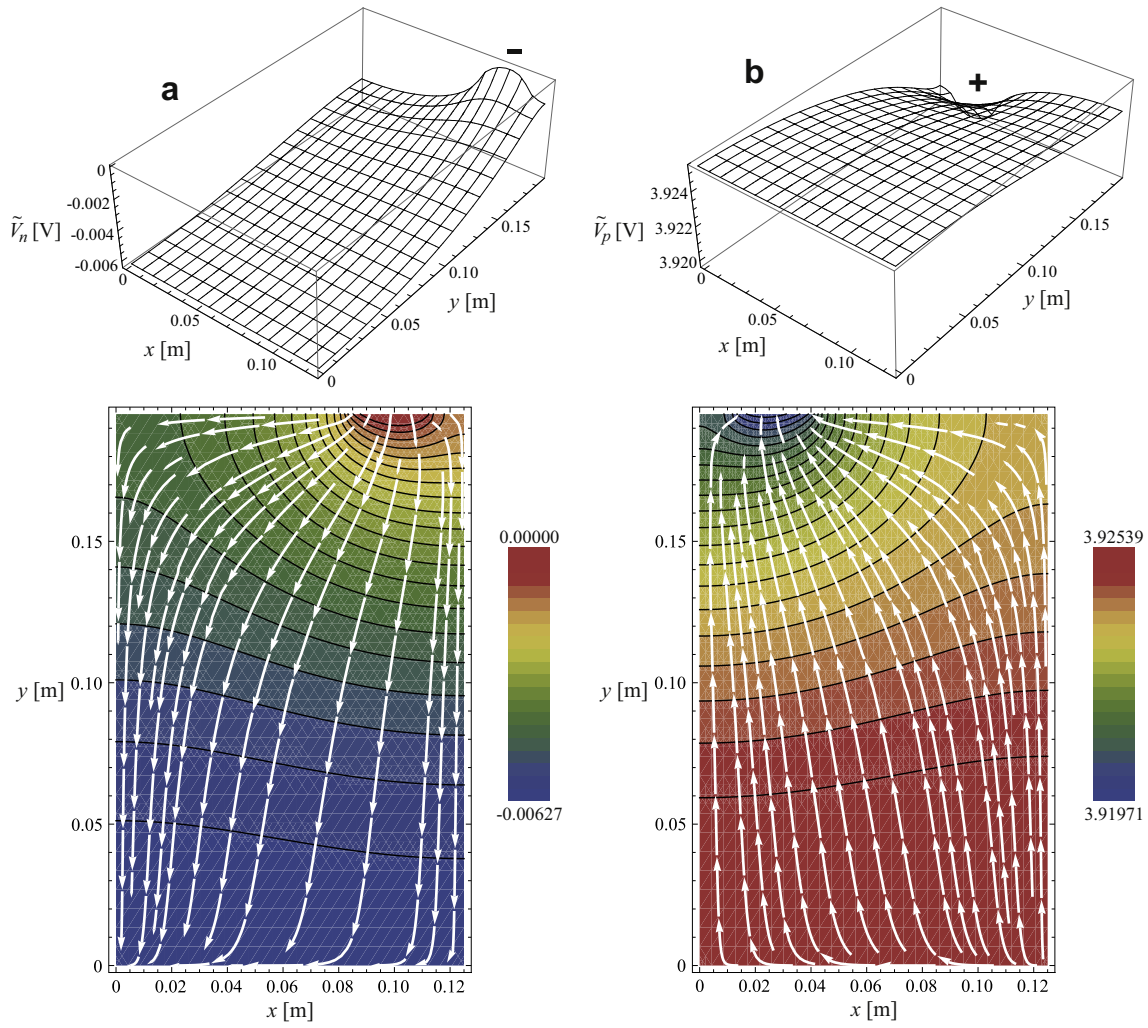

Fig. 13. The potential distribution on negative electrode (plot a) and positive electrode (plot b), obtained from the proposed analytical model, is shown during a 3C-rate discharge process at DOD = 5%.

Similar to the numerical approach, the battery voltage with respect to DOD can be evaluated as

$$V_{\text{batt}} = \frac{1}{b}\int_{e_p-\frac{b}{2}}^{e_p+\frac{b}{2}} \tilde{V}_p(x,c)\,dx \tag{26}$$

Using the analytic approach, the authors reproduced battery discharge curves versus DOD with the same accuracy as of the numerical model; see Fig. 8. To avoid duplicated figures the results are not shown. In Fig. 13, potential distributions on positive and negative electrodes, obtained from the analytical model, are shown at $t = 60$s (DOD = 5%) during a 3C-rate discharge process. The results show satisfactory agreement with the numerical data in Fig. 9. The minor difference between the magnitude of potential distribution in analytical and numerical models corresponds to the assumption of a uniform reaction current $\bar{J}$ in the analytic model instead of a distributed reaction current $J(x, y)$, and also the differences in setting the reference electrode in analytical and numerical approaches.

Figure 14 shows the magnitude of in-plane current density distribution on negative and positive electrodes, obtained analytically from Eq. (14). The results show fair agreement with the numerical data in Fig. 10. In contrast to the numerical model, in the analytical model since tab boundary conditions are the same [cf. Eq. (17d)] the current distribution at the vicinity of the tabs turn out to be similar.

Both numerical and analytical computations were performed on a PC with 8GB of RAM and a 2.50GHz dual core x64-based CPU (Intel Core i5-3210M Processor). Due to the absence of sharp voltage gradients in the solution, the numerical solution is not very sensitive to the resolution of the computational grid. The difference between calculated voltages with a fine grid (4500 elements) and a relatively coarse grid (800 elements) was in the order of 0.1 millivolt, while the relative tolerance was set to 10^{-6}. For the case of 3C-rate charging (a 20-minute process) the numerical simulation time was 36 seconds for the fine grid and 11 seconds for the coarse grid. For lower discharge rates the computational time increases in proportion with the actual process time. The analytical solution with a list of 1000 eigenvalues takes less than a second to complete. It is important to mention that unlike numerical simulations, the computational time in analytical simulations is independent of the actual process time.

7. Summary and Conclusions

The distributions of current and potential on electrodes of Li-ion batteries with planar tabbed configuration are studied. A pouch type Li-ion battery (20 Ah) is characterized experimentally to obtain its polarization expressions during constant current discharge processes. The time dependence behaviour of

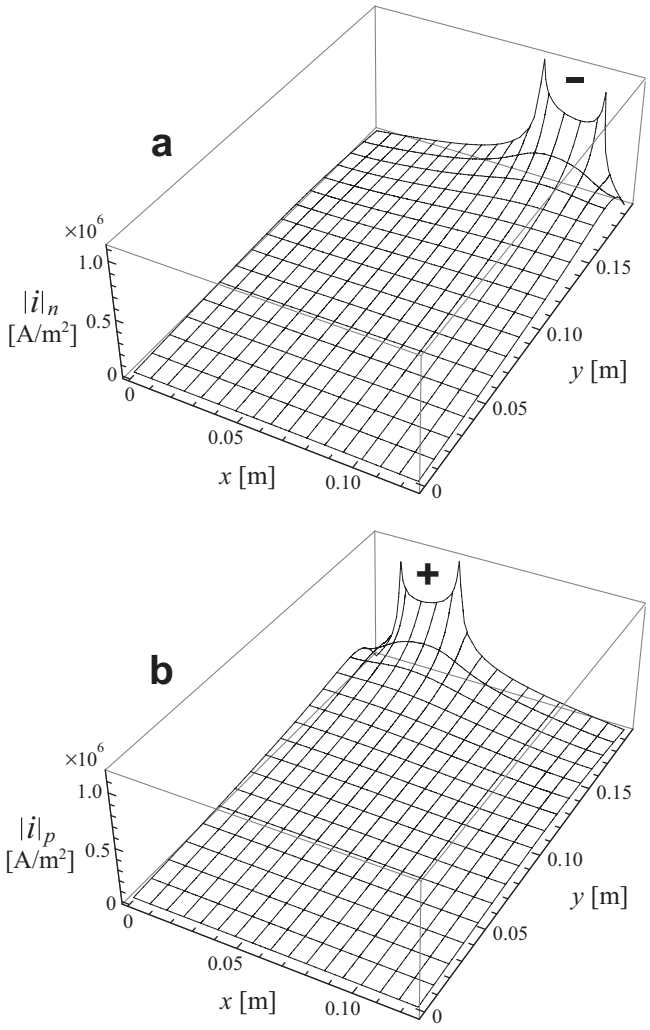

Fig. 14. The in-plane current distribution on positive and negative electrodes, obtained from the proposed analytical model, are shown during a 3C-rate discharge.

the battery during galvanostatic discharge processes is simulated numerically to investigate the potential and current distributions on its electrodes and distribution of the reaction current between its electrodes.

Numerical simulations suggest that a uniformly distributed reaction current can be assumed between the electrodes. Based on this assumption, the governing equations for positive and negative electrodes are decoupled and an analytical model is developed to describe two-dimensional distributions of current and potential on the electrodes. The analytical model takes a series-form solution and yields excellent agreement with experimental and numerical data at a small computational cost.

Deviations of the battery voltage, V_{batt}, from the equilibrium voltage, V_{oc}, can be divided into: *i*) through-plane electrochemical resistance between the electrodes, and *ii*) in-plane electrical resistance on the electrodes. The results of this study confirms that contributions of in-plane resistances to voltage drop are in general much smaller compared to the through-plane resistance. Nonetheless, large potential gradients can be established locally, due to current constriction near the tabs [27], which is an important phenomena from the thermal management point of view. Experimental observations confirm that, temperature at the vicinity of the tabs is higher compared to other parts of the battery, which is the direct result of increased current density at the tab [28,35].

The mathematical procedure presented in this study, provides a fast yet accurate method to investigate the effects of electrodes geometry on potential and current distributions. Furthermore, the proposed electrical model can be coupled to a multi-dimensional thermal model [41] to form an analytical electro-thermal model.

Acknowledgment

The authors from Laboratory for Alternative Energy Conversion (LAEC) thank Automotive Partnership Canada (APC) for the financial supported of this project, Grant No. APCPJ 401826-10.

References

[1] J. Newman, K.E. Thomas-Alyea, Electrochemical systems, 3rd Edition, John Wiley & Sons, New Jersey, 2004.
[2] M. Doyle, T.F. Fuller, J. Newman, Modeling of galvanostatic charge and discharge of the lithium/polymer/insertion cell, Journal of The Electrochemical Society 140 (1993) 1526.
[3] T.F. Fuller, M. Doyle, J. Newman, Simulation and optimization of the dual lithium ion insertion cell, Journal of The Electrochemical Society 141 (1994) 1.
[4] M. Doyle, J. Newman, A.S. Gozdz, C.N. Schmutz, J. Tarascon, Comparison of modeling predictions with experimental data from plastic lithium ion cells, Journal of The Electrochemical Society 143 (1996) 1890.
[5] Y. Ye, Y. Shi, N. Cai, J. Lee, X. He, Electro-thermal modeling and experimental validation for lithium ion battery, Journal of Power Sources 199 (2012) 227.
[6] K. Somasundaram, E. Birgersson, A.S. Mujumdar, Thermal-electrochemical model for passive thermal management of a spiral-wound lithium-ion battery, Journal of Power Sources 203 (2012) 84.
[7] S. Elul, Y. Cohen, D. Aurbach, The influence of geometry in 2d simulation on the charge/discharge processes in li-ion batteries, Journal of Electroanalytical Chemistry 682 (2012) 53.
[8] L. Cai, Y. Dai, M. Nicholson, R.E. White, K. Jagannathan, G. Bhatia, Life modeling of a lithium ion cell with a spinel-based cathode, Journal of Power Sources 221 (2013) 191.
[9] N. Baba, H. Yoshida, M. Nagaoka, C. Okuda, S. Kawauchi, Numerical simulation of thermal behavior of lithium-ion secondary batteries using the enhanced single particle model, Journal of Power Sources 252 (2014) 214.
[10] K. Smith, C.-Y. Wang, Power and thermal characterization of a lithium-ion battery pack for hybrid-electric vehicles, Journal of Power Sources 160 (2006) 662.
[11] R.E. Gerver, J.P. Meyers, Three-dimensional modeling of electrochemical performance and heat generation of lithium-ion batteries in tabbed planar configurations, Journal of The Electrochemical Society 158 (2011) A835.
[12] G.-H. Kim, K. Smith, K.-J. Lee, S. Santhanagopalan, A. Pesaran, Multi-domain modeling of lithium-ion batteries encompassing multi-physics in varied length scales, Journal of The Electrochemical Society 158 (2011) A955.
[13] M. Guo, R.E. White, A distributed thermal model for a li-ion electrode plate pair, Journal of Power Sources 221 (2013) 334.
[14] T.-S. Dao, C.P. Vyasarayani, J. McPhee, Simplification and order reduction of lithium-ion battery model based on porous-electrode theory, Journal of Power Sources 198 (2012) 329.
[15] T.R. Ferguson, M.Z. Bazant, Nonequilibrium thermodynamics of porous electrodes, Journal of Electrochemical Society 159 (2012) A1967.
[16] V.R. Subramanian, V. Boovaragavan, V.D. Diwakar, Toward real-time simulation of physics based lithium-ion battery models, Electrochemical and Solid-State Letters 10 (2007) A255.
[17] X. Li, M. Xiao, S.-Y. Choe, Reduced order model (rom) of a pouch type lithium polymer battery based on electrochemical thermal principles for real time applications, Electrochimica Acta 97 (2013) 66.
[18] V. Ramadesigan, P.W.C. Northrop, S. De, S. Santhanagopalan, R.D. Braatz, V.R. Subramanian, Modeling and simulation of lithium-ion batteries from a systems engineering perspective, Journal of the Electrochemical Society 159 (2012) R31.
[19] K.A. Smith, C.D. Rahn, C.-Y. Wang, Model-based electrochemical estimation and constraint management for pulse operation of lithium ion batteries, IEEE Transactions on Control Systems Technology 18 (2010) 654.
[20] S. Jung, D. Kang, Multi-dimensional modeling of large-scale lithium-ion batteries, Journal of Power Sources 248 (2014) 498.
[21] M.W. Verbrugge, R.S. Conell, Electrochemical and thermal characterization of battery modules commensurate with electric vehicle integration, Journal of the Electrochemical Society 149 (2002) A45.
[22] M.W. Verbrugge, P. Liu, Electrochemical characterization of high-power lithium ion batteries using triangular voltage and current excitation sources, Journal of Power Sources 174 (2007) 2.
[23] W. Tiedemann, J. Newman, in: S. Gross (Ed.), Battery design and optimization, The Electrochemical Society Proceeding Series, Pennington, NJ, 1979, p. 39.
[24] H. Gu, Mathematical analysis of a Zn/NiOOH cell, Journal of the Electrochemical Society 130 (1983) 1459.
[25] J. Newman, W. Tiedemann, Potential and current distribution in electrochemical cells: Interpretation of the half-cell voltage measurements as a function of reference-electrode location, Journal of the Electrochemical Society 140 (1993) 1961.

[26] K.H. Kwon, C.B. Shin, T.H. Kang, C.-S. Kim, A two-dimensional modeling of a lithium-polymer battery, Journal of Power Sources 163 (2006) 151.
[27] P. Taheri, A. Mansouri, B. Schweitzer, M. Yazdanpour, M. Bahrami, Electrical constriction resistance in current collectors of large-scale lithium-ion batteries, Journal of the Electrochemical Society 160 (2013) A1731.
[28] U.S. Kim, C.B. Shin, C.-S. Kim, Effect of electrode configuration on the thermal behavior of a lithium-polymer battery, Journal of Power Sources 180 (2008) 909.
[29] U.S. Kim, C.B. Shin, C.-S. Kim, Modeling for the scale-up of a lithium-ion polymer battery, Journal of Power Sources 189 (2009) 841.
[30] U.S. Kim, J. Yi, C.B. Shin, T. Han, S. Park, Modeling the dependence of the discharge behavior of a lithium-ion battery on the environmental temperature, Journal of the Electrochemical Society 158 (2011) A611.
[31] J. Yi, U.S. Kim, C.B. Shin, T. Han, S. Park, Three-dimensional thermal modeling of a lithium-ion battery considering the combined effects of the electrical and thermal contact resistances between current collecting tab and lead wire, Journal of the Electrochemical Society 160 (2013) A437.
[32] S. Chacko, Y.M. Chung, Thermal modelling of li-ion polymer battery for electric vehicle drive cycles, Journal of Power Sources 213 (2012) 296.
[33] S. Chen, C. Wan, Y. Wang, Thermal analysis of lithium-ion batteries, Journal of Power Sources 140 (2005) 111.
[34] G.-H. Kim, A. Pesaran, R. Spotnitz, A three-dimensional thermal abuse model for lithium-ion cells, Journal of Power Sources 170 (2007) 476.
[35] U.S. Kim, J. Yi, C.B. Shin, T. Han, S. Park, Modelling the thermal behaviour of a lithium-ion battery during charge, Journal of Power Sources 196 (2011) 5115.
[36] J. Yi, U.S. Kim, C.B. Shin, T. Han, S. Park, Modeling the temperature dependence of the discharge behavior of a lithium-ion battery in low environmental temperature, Journal of Power Sources 244 (2013) 143.
[37] S. Szpak, C.J. Gabriel, J.R. Driscoll, Catastrophic thermal runaway in lithium batteries, Electrochimica Acta 32 (1987) 239.
[38] M. Doyle, J. Newman, Analysis of capacity-rate data for lithium batteries using simplified models of the discharge process, Journal of Applied Electrochemistry 27 (1997) 846.
[39] H.S. Carslaw, J.C. Jaeger, Conduction of heat in solids, 2nd Edition, Clarendon Press, Oxford, 1959.
[40] M.N. Özisik, Boundary value problems of heat conduction, DoverPublications, New York, 1989.
[41] P. Taheri, M. Yazdanpour, M. Bahrami, Transient three-dimensional thermal model for batteries with thin electrodes, Journal of Power Sources 243 (2013) 280.